RSC Advances

PAPER

View Article Online
View Journal | View Issue

Cite this: *RSC Adv.*, 2017, **7**, 31448

Magnetically separable AgI–BiOI/$CoFe_2O_4$ hybrid composites for Hg^0 removal: characterization, activity and mechanism

Lixiang Zhang,[a] Anchao Zhang,*[a] Hao Lu,[a] Zhijun Sun,[ab] Wei Sheng,[a] Lushi Sun[b] and Jun Xiang*[b]

A series of magnetically separable AgI–BiOI/$CoFe_2O_4$ hybrid composites were successfully synthesized *via* a solvothermal and subsequent coprecipitation method. The microstructure and magnetism of the materials were characterized by X-ray diffraction (XRD), N_2 adsorption–desorption, scanning electron microscopy (SEM), transmission electron microscopy (TEM), high-resolution transmission electron microscopy (HRTEM), X-ray photoelectron spectroscopy (XPS), UV-vis diffuse reflectance spectroscopy (DRS), photocurrent test, electron spin resonance (ESR) and vibrating sample magnetometer (VSM). The photocatalytic performance of AgI–BiOI/$CoFe_2O_4$ composites on Hg^0 removal from simulated flue gas was carefully designed and evaluated under fluorescent light (FSL) irradiation. The results showed that AgI–BiOI/$CoFe_2O_4$ composites displayed superior photocatalytic activities because of the synergistic effects between AgI, BiOI, and $CoFe_2O_4$ under FSL irradiation. The optimal weight ratio between AgI and the total weight of AgI–BiOI/$CoFe_2O_4$ photocatalyst was 0.3. The presence of a small amount of SO_2 had a dramatic inhibition on Hg^0 removal, while the inhibitory effect of NO on Hg^0 removal could only be observed at a higher NO concentration. The trapping experiments indicated that photoinduced holes (h^+) and superoxide radicals ($^{\bullet}O_2^-$) were the primary active substances in the AgI–BiOI/$CoFe_2O_4$ photocatalytic oxidation system. According to the experimental and characterization results, one plausible mechanism for enhanced Hg^0 removal performance over AgI–BiOI/$CoFe_2O_4$ composites was proposed.

Received 12th April 2017
Accepted 14th June 2017

DOI: 10.1039/c7ra04175f

rsc.li/rsc-advances

1. Introduction

Mercury has received great attention owing to its toxicity, persistence and bioaccumulation in recent years.[1,2] Coal-fired power plants are thought to be responsible for most of the anthropogenic mercury emissions into the environment.[3,4] In 2011, the State Environmental Protection Administration of China issued a new national standard to specify the emission limits of mercury and its compounds from coal-fired flue gas.[5] In China, coal accounts for about 70% of the total primary energy consumption.[6] Mercury from flue gases often exists as elemental mercury (Hg^0), oxidized mercury (Hg^{2+}) and particulate mercury (Hg^p).[7] Compared with Hg^{2+} and Hg^p, Hg^0 is hardly removed owing to its volatility and indissolubility.[8] To meet the increasingly severe emission standards, it is urgent to effectively remove Hg^0 from coal-fired power plants.

In recent years, wet catalytic oxidation technology including UV/fenton,[9] UV/H_2O_2,[10] H_2O_2/$Na_2S_2O_8$,[11] $NaClO_2$,[12] and gas-phase photocatalytic oxidation with TiO_2,[13] SiO_2–TiO_2,[14] CuO/TiO_2,[15] TiO_2–aluminum silicate fiber,[16] and $BiOIO_3$,[17] as photocatalysts have been explored extensively to remove Hg^0 from flue gas. Most of these technologies can effectively remove Hg^0 with the aid of UV energy.[9,13–17] Under UV light irradiation, the produced reactive species such as hydroxyl radicals ($^{\bullet}OH$) and hydroperoxyl radicals ($^{\bullet}HO_2$) possessing higher oxidability would oxidize Hg^0 into Hg^{2+}. This technique is promising since it could be carried out at low temperatures. However, the method needs lots of UV light irradiation and H_2O_2 or with the assistance of TiO_2. Moreover, TiO_2 itself has a large band gap (about 3.2 eV), which could only be excited under UV light to produce some useful reactive substances. The high cost of supplying successive UV light in coal-fired power plant limits its practical application. To solve this problem, it is urgent to fabricate a novel photocatalyst that can generate reactive species under visible light or even sunlight irradiation.

To date, a lot of novel Ag-based and Bi-based photocatalytic materials have been employed as efficient visible-light-responsive photocatalysts, such as Ag_2CO_3,[18] Ag_3PO_4,[19] Ag–AgI/Al_2O_3,[20] BiOX (X = Cl, Br, I),[21] AgI/BiOI,[22] and AgI/Bi_5O_7I.[23]

[a]*School of Mechanical and Power Engineering, Henan Polytechnic University, Jiaozuo, 454000, China. E-mail: anchaozhang@126.com; Fax: +86 391 3987511; Tel: +86 391 3987511*

[b]*State Key Laboratory of Coal Combustion, Huazhong University of Science and Technology, Wuhan, 430074, China. E-mail: xiangjun@mail.hust.edu.cn; Fax: +86 27 87545526; Tel: +86 27 87545526*

During the photocatalytic oxidation processes, large amounts of reactive substances such as holes (h^+), superoxide radicals ($^{\bullet}O_2^-$) and $^{\bullet}OH$ were generated. Hg^0 could be possibly oxidized by these radicals due to their superior oxidation ability. To realize the above inference, the activity of Hg^0 removal using visible-light-driven Ag/AgI–Ag_2CO_3 photocatalyst was investigated tentatively in our previous studies.[24] The results indicated that this photocatalytic oxidation technology can effectively remove Hg^0 under fluorescent light. Moreover, this technology can combine with wet flue gas desulfurization system (WFGD) to simultaneously remove Hg^0 and SO_2 at relatively low temperature, which brings out us a new insight into Hg^0 removal from flue gas.

Although photocatalysis is efficient under fluorescent light, however, the applications of this type of powder photocatalysts also face a major bottleneck such as separation and cyclic utilization.[25,26] In consideration of the easy separation of powder photocatalysts from reaction solution, a useful strategy to integrate Ag-based or Bi-based composites with magnetic nanoparticles such as Fe_3O_4,[27] $CoFe_2O_4$,[28] $ZnFe_2O_4$,[29] $NiFe_2O_4$,[30] and $SrFe_{12}O_{19}$,[31] was proposed. Among the magnetic materials, $CoFe_2O_4$ has been widely employed in photocatalytic degradation of organic pollutants due to its small band gap energy and moderate saturation magnetization.[28,32] Moreover, it also was reported that there were significant synergistic effects of individual components in $CoFe_2O_4$-based nanocomposites. For example, when active components such as BiOBr,[33] $BiVO_4$,[34] ZnO,[35] CdS,[36] and Ag/Ag_3VO_4,[37] were combined with $CoFe_2O_4$ respectively and employed in photocatalytic degradation of organic pollutants, the hybrid composites all showed enhanced photocatalytic activities than single component under visible light irradiation, and more importantly, they could be used for many times and recovered easily by an external magnetic force.

Thus, to reduce the cost of photocatalyst and obtain better photocatalytic activity with easy recovery, in this work, a series of novel magnetically separable AgI–BiOI/$CoFe_2O_4$ hybrids with lower silver content were synthesized *via* a solvothermal and subsequent coprecipitation method to remove Hg^0 under fluorescent light (FSL) irradiation, which has not yet been researched in the literatures. As was expected, the as-synthesized ternary AgI–BiOI/$CoFe_2O_4$ composites displayed higher Hg^0 removal activity than single component $CoFe_2O_4$ and BiOI under fluorescent light. The cyclic experiment showed that the optimal hybrid had stable photocatalytic activity and was relatively stable in crystal structures in the photocatalytic process. The synthesized ternary composite proved to be promising for wet photocatalytic oxidation removal of Hg^0 from flue gas.

2. Experimental

2.1. Synthesis of $CoFe_2O_4$ nanoparticles

The $CoFe_2O_4$ composites were synthesized *via* a solvothermal method.[37] All chemical agents employed were of analytical grade. Typically, 1.24 g of $Co(NO_3)_2 \cdot 6H_2O$ and 3.44 g of $Fe(NO_3)_3 \cdot 9H_2O$ were dissolved into 40 mL deionized water to obtain a mixed solution with magnetic stirring for about 60 min. Then, 30 mL of 1 M NaOH solution was added dropwise into the above mixed solution with stirring for another 60 min. Subsequently, the suspension was placed into a Teflon-lined autoclave (100 mL) and heated at 180 °C for 12 h. The resultant product was allowed to cool down to ambient temperature and then washed with distilled water several times. Finally, the obtained $CoFe_2O_4$ (abbreviated as CFO) composites were dried under vacuum at 60 °C for 12 h.

2.2. Synthesis of AgI–BiOI/$CoFe_2O_4$ microparticles

AgI–BiOI/$CoFe_2O_4$ samples were fabricated *via* a modified coprecipitation method,[38,39] in which the mass ratio of $CoFe_2O_4$ (CFO) and total mass of the photocatalyst was fixed at 20%. Firstly, 4.82 g of $Bi(NO_3)_3 \cdot 5H_2O$ and 0.36 g of $AgNO_3$ were dissolved into 200 mL aqueous solution containing 20 mL acetic acid. Secondly, 1.00 g of as-prepared CFO powder was added into the above solvent with continuous stirring for 60 min. Then, 100 mL of 0.12 M KI solution was added to the above suspension. Finally, after stirring for another 60 min and placed for 12 h, the resulting precipitate was washed with ethanol water mixture for 3–5 times, filtered and dried at 60 °C for 24 h, respectively. The obtained composites were designated as $AgI_{0.1}$BiOI/CFO for simplicity, where the value of 0.1 was the weight ratio between AgI and the total weight of the photocatalyst. Equally, other different photocatalysts were synthesized *via* the same procedure and named as BiOI/CFO, AgI/CFO, $AgI_{0.2}$BiOI/CFO, $AgI_{0.3}$BiOI/CFO, $AgI_{0.4}$BiOI/CFO, and $AgI_{0.5}$-BiOI/CFO. For comparison, pure AgI and BiOI were also synthesized *via* the same method without the addition of $CoFe_2O_4$.

2.3. Characterization of photocatalysts

X-ray powder diffraction (XRD) analyses were performed on a D8 advance diffractometer (Bruker, Germany). N_2 adsorption–desorption tests were carried out on an Autosorb iQ surface area and porosity analyzer (Quantachrome, USA) and the photocatalysts were degassed at 150 °C in vacuum for 8 h before the nitrogen adsorption isotherm was constructed. Scanning electron microscope (SEM) was carried out on a field emission scanning electron microscope (NoVa™ Nano SEM 430, FEI Company). Transmission electron microscope (TEM) and high-resolution transmission electron microscope (HRTEM) analyses were conducted on a Tecnai G20 microscopy (FEI, USA). X-ray photoelectron spectroscopy (XPS) experiments were performed on an Escalab 250xi spectrometer (Thermo Fisher, USA). UV-vis diffuse reflection spectra (DRS) were recorded on an UV2401 spectrophotometer (Shimadzu, Japan). The free radicals were detected on an ER200-SRC electron spin resonance spectrometer (ESR, Bruker, Germany). The magnetism of the composite was analyzed on a MPMS XL-7 magnetometer (Quantum Design, USA).

2.4. Photoelectrochemical measurement

The photoelectrochemical performances of the composites were conducted on a CHI 760E electrochemical work-station (Chenhua, China) in a standard three electrode system using

fabricated photo-anode as the working electrode. A Pt wire and a saturated calomel electrode were respectively utilized as the counter and reference electrode. The 0.5 M Na_2SO_4 solution (pH = 5.8) purged with N_2 was utilized as the electrolyte. A 300 W PLS-SXE300 Xe illuminator with a UV-cutoff filter ($\lambda \geq 420$ nm) was used as the light source.

2.5. Photocatalytic activity test

The photocatalytic performances of as-prepared composites were implemented on a laboratory-scale wet bubbling photocatalytic reactor at ambient temperature. A detailed description about the experimental setup and process was provided in our previous work.[24] In the experiment, the simulated flue gas was composed of 6% of O_2, 12% of CO_2, 55 μg m^{-3} of Hg^0 vapor, and balance N_2. The total flow rate was approximately 1.50 L min^{-1}. 0.2 g of photocatalyst and 1 L of deionized water were uniformly mixed as the reaction solution and the reaction temperature was set as 45 °C. During the test, Hg^0 concentration data was collected by an online VM-3000 mercury analysis instrument. The Hg^0 removal efficiency η (%) was calculated according to the following equation:

$$\eta = (1 - C_{out}/C_{in}) \times 100 \quad (1)$$

where C_{out} and C_{in} represent the outlet and inlet Hg^0 concentrations (μg m^{-3}), respectively.

3. Results and discussion

3.1. Photocatalytic activity

3.1.1. Effect of AgI content. The photocatalytic performances of Hg^0 by as-prepared materials were studied under fluorescent light (FSL) irradiation and the corresponding results were shown in Fig. 1. It can be observed that under FSL irradiation, pure CFO and BiOI could only remove about 6% and 42% of Hg^0 in 60 min, respectively, whereas approximately 68% of Hg^0 was removed by BiOI/CFO. This comparison suggested that BiOI had relatively poor Hg^0 removal ability, but the introduction of magnetic CFO onto BiOI could efficiently enhance its photocatalytic performance. The above phenomena can be explained that because of a small band gap of $CoFe_2O_4$ and a high e^-–h^+ pair recombination rate, pure CFO can hardly oxidize Hg^0 to Hg^{2+}. However, when BiOI was combined with CFO, a more efficient charge separation from BiOI/CFO can be achieved since the introduction of CFO can enhance the photoluminescent intensity of metal oxides.[33,40]

Furthermore, when different amounts of AgI were doped with BiOI/CFO, all ternary AgI–BiOI/CFO composites displayed much higher Hg^0 removal efficiency than BiOI/CFO and the photocatalytic performances of ternary AgI–BiOI/CFO composites depended on AgI content. The $AgI_{0.3}$BiOI/CFO exhibited the highest Hg^0 removal efficiency (99%) when the weight ratio between AgI and AgI–BiOI/CFO was increased from 10% to 50%. It was reported that the composites with multifunctional components could combine individual advantages to achieve a high photocatalytic performance.[41] Thus, a much better Hg^0 removal efficiency could be obtained for AgI–BiOI/CFO hybrids.

3.1.2. Effect of FSL illumination. Fig. 2 shows the effect of FSL illumination on Hg^0 removal efficiency. It was clear that only about 5% and 35% of Hg^0 removal efficiencies were observed only with FSL irradiation and only with $AgI_{0.3}$BiOI/CFO, respectively, indicating that Hg^0 cannot be easily removed without FSL irradiation or photocatalyst. However, once both $AgI_{0.3}$BiOI/CFO composite and FSL irradiation were employed simultaneously in the reaction system, Hg^0 removal efficiency dramatically increased to about 99%. The enhanced Hg^0 removal activity could be evidently due to the synergistic effect of $AgI_{0.3}$BiOI/CFO and FSL irradiation.

3.1.3. Effect of flue gas composition. In the coal-fired power plants, actual exhaust gas inevitably contained some concentrations of SO_2 and NO, which may exert inhibitory or promotional impacts on Hg^0 removal. Fig. 3 shows the effects of SO_2 and NO concentrations on Hg^0 removal. When 200 ppm of SO_2 was introduced into the reaction stream in the ranges of 30–60 and 90–120 min, greater inhibitory effects on Hg^0 removal appeared. However, when 100 and 200 ppm of NO were added, there was almost no loss in Hg^0 removal efficiency, but a decrement of Hg^0 removal efficiency from 93% to 75% was observed when NO concentration further increased to 600 ppm. Moreover, once SO_2 and NO were cut off, the removal efficiency of Hg^0 restored to about its initial value, suggesting that the structure of the photocatalyst had not been destroyed by SO_2 and NO. According to previous reports,[9,42] the inhibition could

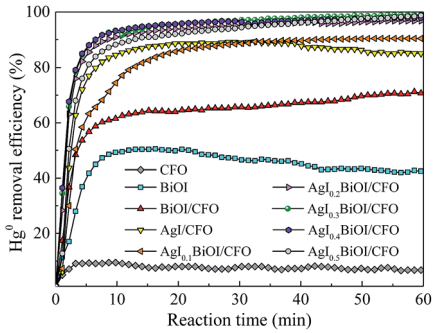

Fig. 1 Effect of AgI content on Hg^0 removal efficiency.

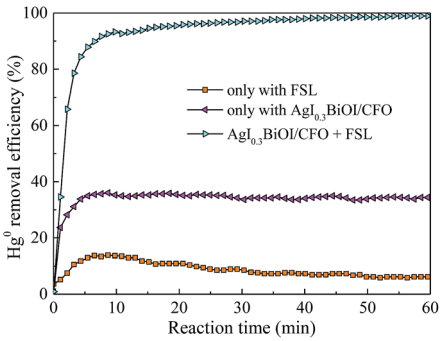

Fig. 2 Effect of FSL irradiation on Hg^0 removal efficiency.

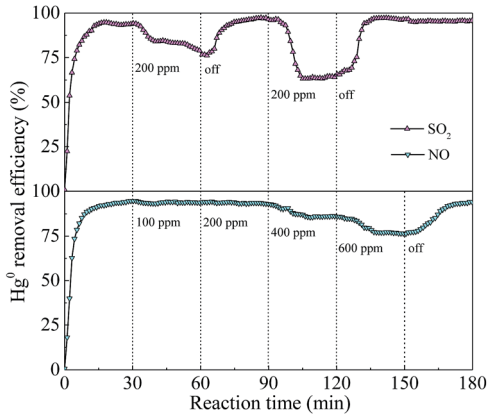

Fig. 3 Effect of SO_2 and NO on Hg^0 removal efficiency.

be ascribed to the consumption of photogenerated reactive species by SO_2 and NO.

3.2. Photocatalyst characterization

3.2.1. XRD and N_2 adsorption–desorption. The XRD patterns of $CoFe_2O_4$ (CFO), BiOI, AgI, and AgI–BiOI/$CoFe_2O_4$ samples with differing AgI content were shown in Fig. 4. The diffraction peaks shown in Fig. 4a–c were assigned to the signal phase of $CoFe_2O_4$ (JCPDS 22-1086), tetragonal BiOI (JCPDS 73-2062) and hexagonal AgI (JCPDS 09-0374), respectively.[22,43,44] By comparison, the diffraction intensities of BiOI in BiOI/CFO (Fig. 4d) and AgI in AgI/CFO (Fig. 4e) greatly decreased, suggesting the presence of $CoFe_2O_4$. It was clear that the diffraction patterns of AgI intensified gradually with the increasing of AgI/(AgI–BiOI/CFO) weight ratio (Fig. 4f–j), and the peak intensities of BiOI accordingly weakened. Moreover, two weak diffraction peaks of $CoFe_2O_4$ located at $2\theta = 35.51°$ and 42.67° were

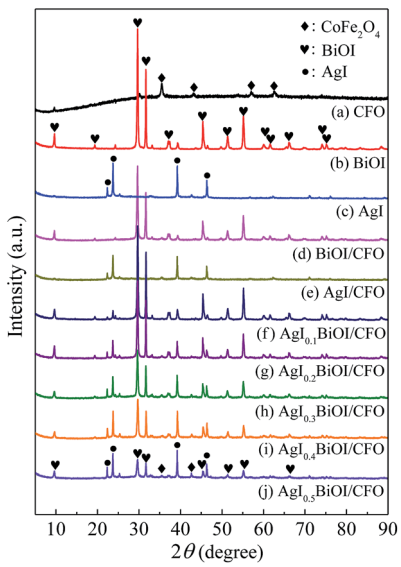

Fig. 4 XRD patterns of the photocatalysts.

Table 1 Physical features of the selected composites

Sample	BET surface area ($m^2\ g^{-1}$)	Total pore volume ($cm^3\ g^{-1}$)	Average pore diameter (nm)
CFO	55.07	2.61×10^{-1}	20.52
BiOI/CFO	21.28	7.85×10^{-2}	20.49
$AgI_{0.3}$BiOI/CFO	20.74	6.56×10^{-2}	17.28

observed from XRD patterns of Fig. 4f–j, indicating the coexistence of AgI, BiOI, and $CoFe_2O_4$ in AgI–BiOI/$CoFe_2O_4$ samples.

Table 1 summarizes the physical features of selected composites. Obviously, CFO showed the largest BET surface area, total pore volume, and average pore diameter among the three samples. When BiOI itself or both BiOI and AgI were combined with CFO, the BET surface areas and total pore volumes of BiOI/CFO and $AgI_{0.3}$BiOI/CFO were greatly decreased, which indicated that BiOI and AgI were successfully doped with CFO.

3.2.2. SEM, TEM and HRTEM. The morphology features of selective composites were analyzed by SEM, TEM and HRTEM. As shown in Fig. 5, CFO exhibited a rough irregular surface, while when AgI was combined with $CoFe_2O_4$, many AgI granules with smooth surface (see red circular marks) appeared. As for BiOI/CFO, the petal-like BiOI particles (see blue circular mark) were observed (Fig. 5c). From Fig. 5d, it can be seen that the petal-like BiOI particles in $AgI_{0.3}$BiOI/CFO composites became dispersed and somehow smaller than BiOI/CFO after the introduction of AgI. To provide the evidence that AgI and BiOI particles were successfully mixed with magnetic CFO, the TEM and HRTEM images of CFO and $AgI_{0.3}$BiOI/CFO were investigated. The TEM images shown in Fig. 5e and f indicated that the $CoFe_2O_4$ grains were uniformly distributed on the surface of $AgI_{0.3}$BiOI/CFO photocatalyst. The lattice spacing belonged to (311) plane of CFO was observed (Fig. 5g), while as for $AgI_{0.3}$-BiOI/CFO (Fig. 5f), three different lattice spacings were observed. The lattice spacings of 0.25, 0.27 and 0.30 nm corresponded to the (311) plane of CFO, (102) plane of AgI and (102) plane of BiOI, respectively, which further indicated that BiOI and AgI were successfully doped with CFO.[36,45]

3.2.3. XPS. To obtain the surface compositions and chemical status of the as-prepared samples, XPS technique was employed and the corresponding results were displayed in Fig. 6. Fig. 6a exhibits the XPS spectra of Bi 4f. For BiOI/CFO, the peaks located at 164.49 and 159.15 eV were belonged to Bi $4f_{5/2}$ and Bi $4f_{7/2}$,[46] while the peaks of Bi $4f_{5/2}$ and Bi $4f_{7/2}$ from $AgI_{0.3}$BiOI/CFO shifted to higher binding energy. Fig. 6b shows the XPS spectra of I 3d. The peaks in BiOI/CFO centered at 630.33 and 618.93 eV corresponded to the spectrums of I $3d_{3/2}$ and I $3d_{5/2}$,[47] while for AgI/CFO and $AgI_{0.3}$BiOI/CFO, their peaks of I $3d_{3/2}$ and I $3d_{5/2}$ all shifted to higher binding energies. The peaks belonged to Ag $3d_{3/2}$ and Ag $3d_{5/2}$ was observed in Fig. 6c. It was noted that the peaks of Ag 3d in $AgI_{0.3}$BiOI/CFO have a red-shift to higher binding energy compared with these of AgI/CFO.

The XPS spectra of Co 2p and Fe 2p were displayed in Fig. 6d and e, respectively. The peaks of both Co 2p and Fe 2p in BiOI/

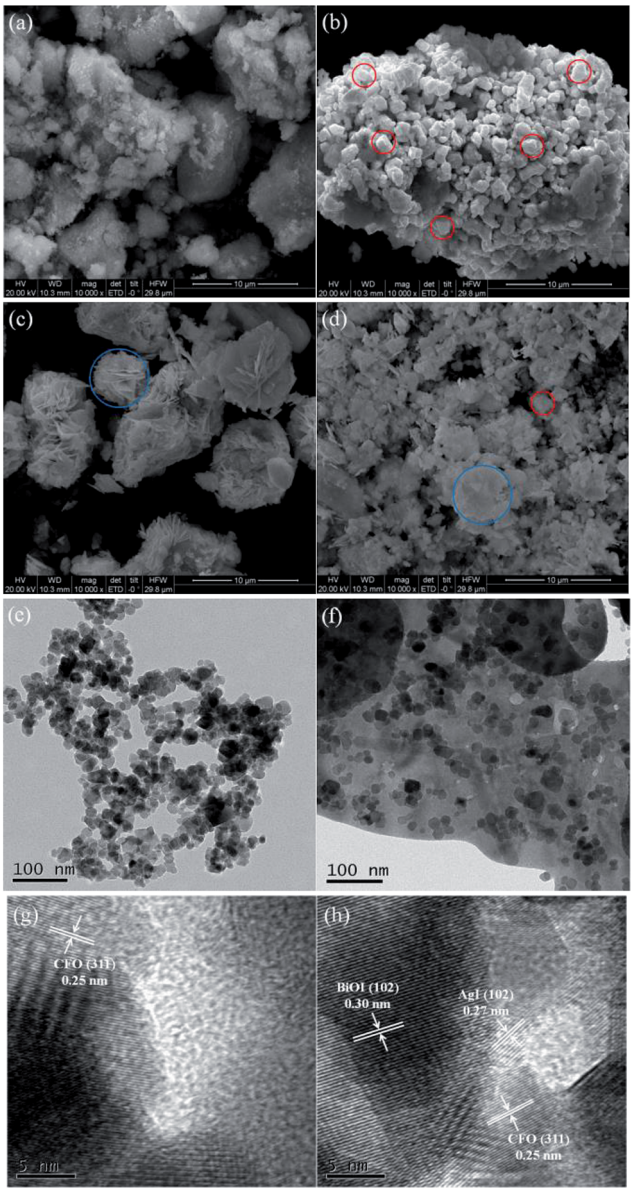

Fig. 5 SEM images of (a) CFO, (b) AgI/CFO, (c) BiOI/CFO and (d) $AgI_{0.3}BiOI/CFO$, TEM images of (e) CFO and (f) $AgI_{0.3}BiOI/CFO$, and HRTEM images of (g) CFO and (h) $AgI_{0.3}BiOI/CFO$.

CFO, AgI/CFO and $AgI_{0.3}BiOI/CFO$ were weaker than that of CFO due to the interposition of CFO into the composites and relatively lower content of CFO. In Fig. 6d, the peaks centered at 797.0 eV (with a satellite peak at 804.50 eV) and 781.8 eV (with a satellite peak at 787.1 eV) were ascribed to Co $2p_{1/2}$ and Co $2p_{3/2}$, which corresponded to the characteristic peaks of Co^{2+} ions in $CoFe_2O_4$.[37] Also, it was observed that the satellite peak of Co $2p_{1/2}$ in BiOI/CFO and $AgI_{0.3}BiOI/CFO$ shifted greatly to higher binding energies. In Fig. 6e, the photoionization region of Fe 2p yielded Fe $2p_{3/2}$ binding energies of 712.32 eV and Fe $2p_{1/2}$ binding energies of 725.84 eV, which is consistent with the Fe 2p binding energy for $CoFe_2O_4$.[37,43] According to previous works,[48,49] all the shifts of binding energy in the XPS spectra can be ascribed to the intense interaction between closely contacted

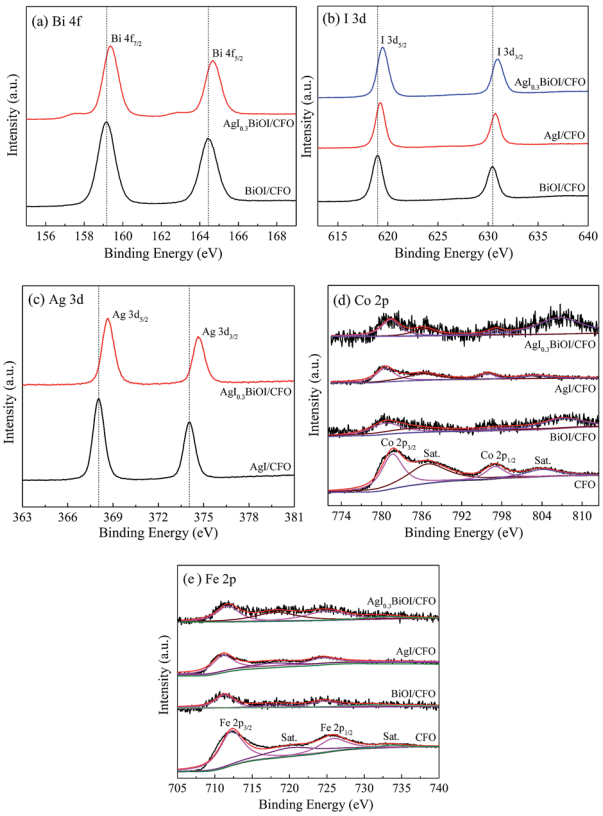

Fig. 6 XPS spectra of the photocatalysts: (a) Bi 4f, (b) I 3d, (c) Ag 3d, (d) Co 2p, and (e) Fe 2p.

phases of AgI, BiOI and CFO, suggesting the successful syntheses of AgI/CFO, BiOI/CFO and $AgI_{0.3}BiOI/CFO$.

3.2.4. DRS. The optical performances of selective composites were performed on a UV-vis spectrophotometer. From Fig. 7a, it was observed that CFO with black surface displayed an almost constant absorption capacity in the wavelength range of 300–800 nm, while pure AgI and BiOI exhibited the absorption edges of around 475 and 670 nm, respectively. When CFO was coupled with AgI and BiOI, the absorption edges of AgI/CFO and BiOI/CFO all shifted to shorter wavelengths than those of pure AgI and BiOI. However, the absorption strengths of AgI/CFO and BiOI/CFO increased in visible region in comparison to AgI and BiOI, indicating the synergistic effect between $CoFe_2O_4$ and AgI or BiOI. When BiOI/CFO was decorated with AgI, the

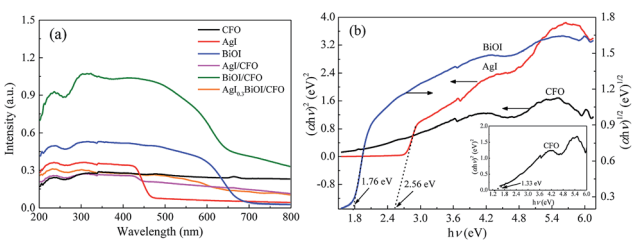

Fig. 7 (a) UV-vis diffuse reflectance spectra of selective samples; (b) plots of $(\alpha h\nu)^2$ *versus* $h\nu$ for AgI, CFO and plot of $(\alpha h\nu)^2$ *versus* $h\nu$ for BiOI.

absorption intensity of $AgI_{0.3}BiOI/CFO$ decreased greatly compared to BiOI/CFO because the band gap of AgI was larger than BiOI.[22] In the photocatalytic process, the component that can absorb more energy was beneficial for the photocatalytic activity of Hg^0 removal to some extent, but the main factor could be the electron–hole (e^-–h^+) pairs separation efficiency of the component.[50,51]

According to the absorption spectra in Fig. 7a, the band gap values of the semiconductors can be measured by the equation as follows:

$$\alpha h\nu = A(h\nu - E_g)^{n/2} \quad (2)$$

where α, h, ν, A, and E_g are the absorption coefficient, Planck constant, light frequency, a proportionality constant, and the band gap, respectively. The value of n depended on the types of photon transition in semiconductors ($n = 1$ for direct transition and $n = 4$ for indirect transition). Thus, the value of n is 1 for direct gap semiconductor AgI and $CoFe_2O_4$ while 4 for indirect gap semiconductor BiOI.[23,37] Hence, as Fig. 7b shows, the band gap energies (E_g) of AgI, BiOI and $CoFe_2O_4$ were estimated to be 2.56, 1.76 and 1.33 eV, respectively. The conduction band (CB) and valence band (VB) values of a semiconductor were measured by the following empirical equations:[22]

$$E_{CB} = X - E^C - 0.5E_g \quad (3)$$

$$E_{VB} = E_{CB} + E_g \quad (4)$$

where E_{CB} and E_{VB} represent the CB and VB potentials, respectively; X is the electronegativity (the X values for AgI, BiOI and $CoFe_2O_4$ are 5.354, 5.941, and 5.815 eV, respectively[22,37]); E^C represents the energy of free electrons on the hydrogen scale (4.5 eV) and E_g refers to the band gap energy of the semiconductor. Thus, the E_{CB} and E_{VB} of the composites were accordingly calculated and summarized in Table 2.

3.2.5. Photocurrent analysis and ESR. The above DRS analysis can be further supported by prompt photocurrent response of the composites under visible light irradiation. In general, the higher the e^-–h^+ pairs separation efficiency, the higher the photocurrent produced, thereby leading to a much higher photocatalytic activity. Fig. 8 compares the prompt photocurrent responses of different samples and a good reproducibility of the photocurrent was observed in several on/off cycling tests. The photocurrent of BiOI/CFO was steadier than those of AgI/CFO and $AgI_{0.3}BiOI/CFO$, implying that there was little recombination process within the whole irradiation period. In comparison to BiOI/CFO and AgI/CFO,

Table 2 Band gap, conduction and valence band of the samples

Sample	Band gap, E_g (eV)	Conduction band, E_{CB} (eV)	Valence band, E_{VB} (eV)
AgI	2.56	−0.43	2.13
BiOI	1.76	0.56	2.32
$CoFe_2O_4$	1.33	0.65	1.98

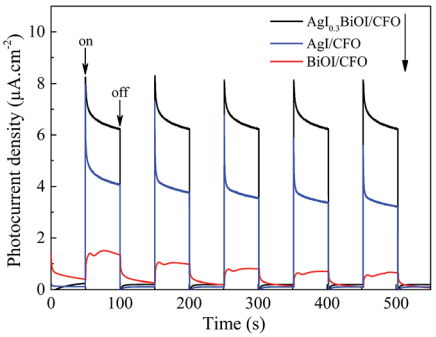

Fig. 8 Prompt photocurrent responses of the samples under visible light irradiation.

$AgI_{0.3}BiOI/CFO$ photocatalyst exhibited much higher photocurrents density. This suggested that the e^-–h^+ pairs separation performance in the photo-electrochemical process of $AgI_{0.3}BiOI/CFO$ had been promoted, which could be ascribed to the appropriate energy band matching between AgI, BiOI and $CoFe_2O_4$.

To explore the reactive substances produced during the photocatalytic oxidation process, ESR technology was utilized and the corresponding result was shown in Fig. 9. Under visible light irradiation, the characteristic peaks of DMPO–$^{\bullet}$OH were detected in the suspension of $AgI_{0.3}BiOI/CFO$, while no such signal appeared in the dark.[52] Furthermore, when $AgI_{0.3}BiOI/CFO$ was dispersed in methanol, DMPO–$^{\bullet}O_2^-$ signals also only appeared under visible light. In the photocatalytic process, $^{\bullet}$OH, $^{\bullet}O_2^-$ and holes played vital roles in pollutant removal.[24,53–55] Thus, the ESR results provided a strong indication that the photogenerated carriers in $AgI_{0.3}BiOI/CFO$ possibly had not only strong redox ability but also survived long enough to react with the absorbed O_2 and OH^- or H_2O to generate reactive $^{\bullet}O_2^-$ and $^{\bullet}$OH.[55]

3.2.6. Magnetic performance. Fig. 10 shows the magnetic hysteresis loops of CFO and $AgI_{0.3}BiOI/CFO$. CFO evidently displayed a strong magnetic response to the varied magnetic field. Since $AgI_{0.3}BiOI/CFO$ only contained 20 wt% of CFO and the components of AgI and BiOI have no magnetism, the magnetic saturation (Ms) value of $AgI_{0.3}BiOI/CFO$ (14.5 emu g^{-1}) was smaller than that of CFO (61.9 emu g^{-1}). However,

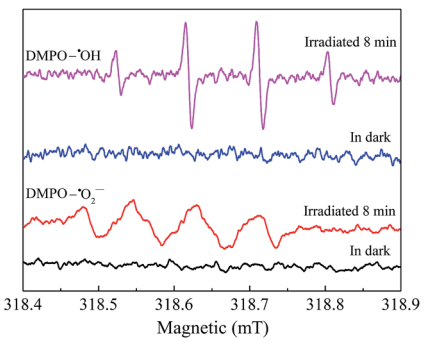

Fig. 9 ESR spectra for DMPO–$^{\bullet}$OH and DMPO–$^{\bullet}O_2^-$ of $AgI_{0.3}BiOI/CFO$.

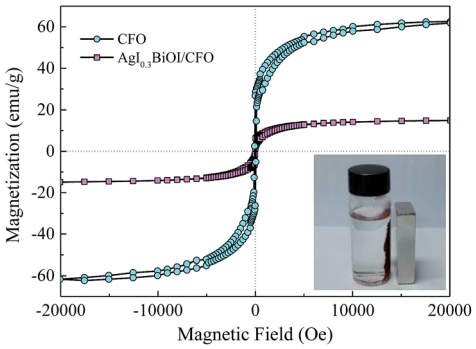

Fig. 10 Magnetization curves of CFO and $AgI_{0.3}BiOI/CFO$.

from the inset of Fig. 10, it found that $AgI_{0.3}BiOI/CFO$ demonstrated a relatively strong enough magnetic separation performance and could be employed as a promising magnetic photocatalyst in the future.

3.3. Mechanism study

The trapping experiments for reactive radicals were performed to clarify the functions of photogenerated e^-–h^+ pairs during Hg^0 removal process. It should be noticed that prior to turning on the light source, 15 mL of isopropyl alcohol (IPA), 0.8 g of ethylene diamine tetraacetic acid disodium salt (EDTA–2Na) and 0.8 g of benzoquinone (BQ) were added along with 0.2 g $AgI_{0.3}BiOI/CFO$ composite into the reaction liquid as the scavenger of $^{\cdot}OH$, h^+ and $^{\cdot}O_2^-$, respectively.[24] As shown in Fig. 11, the Hg^0 removal efficiency of $AgI_{0.3}BiOI/CFO$ decreased by about 7% in the presence of IPA when compared to that of without any scavenger, indicating that $^{\cdot}OH$ radicals had little impact on Hg^0 removal. In contrast, an obvious reduction and a drastic inhibition were observed after the addition of EDTA–2Na and BQ, respectively, implying that h^+ and $^{\cdot}O_2^-$ radicals were the primary reactive substances for Hg^0 removal.

Based on above discussion, a schematic illustration of energy bands matching among AgI, BiOI and $CoFe_2O_4$ and possible ways of charges transfer were depicted in Fig. 12. Under visible light or FSL irradiation, the photoexcited e^-–h^+ pairs would be produced due to lower band gap energies of AgI (2.56 eV) and BiOI (1.76 eV). Since the CB edge of BiOI was more

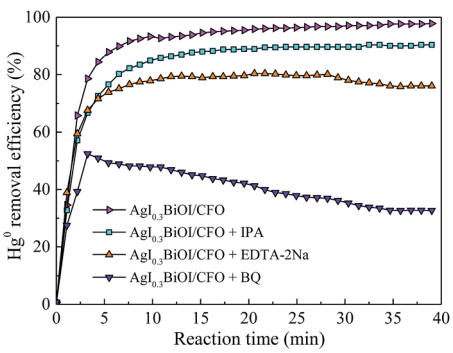

Fig. 11 Effect of different scavengers on Hg^0 removal.

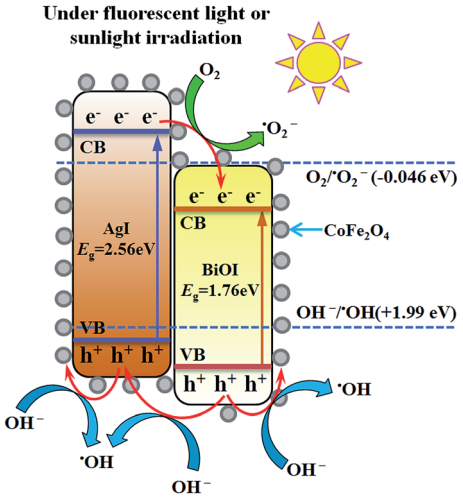

Fig. 12 Schematic mechanism of $AgI_{0.3}BiOI/CFO$ for enhanced Hg^0 removal.

positive than that of AgI, the electrons on the CB of AgI would transfer to the CB of BiOI. Because the VB potential of AgI was more negative than that of BiOI correspondingly, the holes on the VB of BiOI would migrate to the VB of AgI.[22,47] For BiOI and AgI, the electrons on the CB potential of AgI can be trapped by adsorbed O_2 to generate $^{\cdot}O_2^-$ since the CB potential of AgI was more negative than single electron reduction potential of O_2 (-0.046 eV *vs.* NHE).[47] The OH^- or H_2O can be oxidized by holes to yield $^{\cdot}OH$ radicals since the VB potential of BiOI and AgI was more positive than $^{\cdot}OH/OH^-$ (1.99 eV *vs.* NHE).[22,24] Moreover, since the CB potential (0.65 eV) and VB potential (1.98 eV) of $CoFe_2O_4$ was between -0.046 and 1.99 eV, the e^-–h^+ pairs did not have enough redox capacity to generate reactive species such as $^{\cdot}OH$ and $^{\cdot}O_2^-$ and were prone to recombine,[38] thus only 6% of Hg^0 removal efficiency was observed for pure CFO. However, due to lower VB potential of CFO than that of AgI and BiOI, the holes on the VBs of AgI and BiOI would transfer to the VB of CFO,[33] thereby facilitating an effective separation of e^-–h^+ pairs and the presence of some amounts of reactive $^{\cdot}OH$. This might be the reason why binary BiOI/CFO and AgI/CFO composite achieved a higher Hg^0 removal efficiency than single component. Taken together, the recombination of photogenerated e^-–h^+ pairs over $AgI_{0.3}BiOI/CFO$ could be greatly suppressed in such a way and much more electrons and holes could react with O_2, OH^- to generate $^{\cdot}O_2^-$ and $^{\cdot}OH$ radicals. In view of photo-electrochemistry, the products such as $^{\cdot}OH$, $^{\cdot}O_2^-$ and h^+ have enough oxidation capability to oxidize Hg^0. Among them, the $^{\cdot}O_2^-$ and h^+ radicals were confirmed to play crucial roles in Hg^0 removal.

3.4. Stability of photocatalyst

To understand the recyclability and durability of composite $AgI_{0.3}BiOI/CFO$, four successive runs of photocatalytic experiments were performed under FSL irradiation. As shown in Fig. 13, $AgI_{0.3}BiOI/CFO$ exhibited a slight decline in Hg^0 removal efficiency with the recycling tests increasing. About 87% of Hg^0

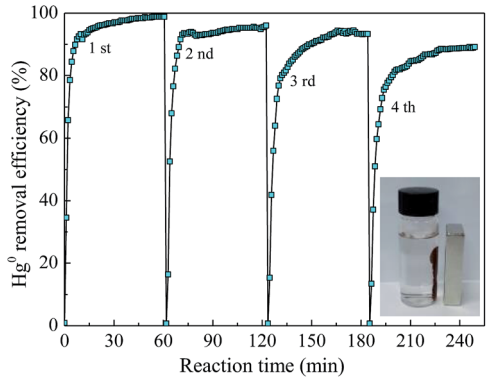

Fig. 13 Hg^0 removal of consecutive experiments by $AgI_{0.3}BiOI/CFO$.

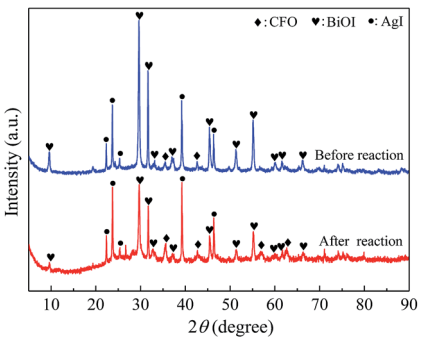

Fig. 14 XRD patterns of $AgI_{0.3}BiOI/CFO$ before and after four successive runs.

removal efficiency was obtained after four successive runs, suggesting that $AgI_{0.3}BiOI/CFO$ was stable during the photocatalytic oxidation process. Furthermore, the inset of Fig. 13 clearly demonstrated that $AgI_{0.3}BiOI/CFO$ after four successive runs still had a good magnetic separation performance. To further investigate the structure change of as-prepared sample after Hg^0 removal test, $AgI_{0.3}BiOI/CFO$ after four successive tests were also characterized by XRD technique. As revealed in Fig. 14, the crystal structure of used $AgI_{0.3}BiOI/CFO$ was almost identical to its fresh sample except two new peaks at 56.94° and 62.68° belonged to $CoFe_2O_4$,[37] indicating a relatively stable crystal structure of the composite in the photocatalytic process.

3.5. Simultaneous removal of SO_2 and Hg^0

Considering that the current mature SCR technology is effective to remove NO and has been widely adopted by power plant, the simultaneous removal of SO_2 and Hg^0 over AgI–BiOI/CFO composite under alkaline condition was preliminary explored. As shown in Fig. 15, when 200 ppm of SO_2 was introduced into the reaction system, Hg^0 removal efficiency has little inhibition and still maintained at 85% with the solution pH adjusted to 11 by adding NaOH solution. Also, nearly 98% of SO_2 removal efficiency was observed, suggesting that a certain degree of alkaline solution can not only restrain the inhibition of SO_2 on Hg^0 removal but also can effectively remove SO_2 from flue gas.

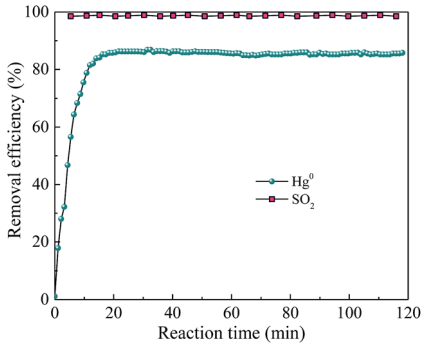

Fig. 15 Simultaneous removal of Hg^0 and SO_2 over $AgI_{0.3}BiOI/CFO$.

4. Conclusions

A series of magnetically separable ternary AgI–BiOI/$CoFe_2O_4$ photocatalysts with different AgI contents were successfully prepared by a solvothermal and sequent coprecipitation method. The as-prepared ternary AgI–BiOI/$CoFe_2O_4$ composites showed greatly enhanced Hg^0 removal activity under FSL irradiation, especially $AgI_{0.3}BiOI/CFO$. $AgI_{0.3}BiOI/CFO$ demonstrated much stable Hg^0 oxidation ability and enough magnetic property to be reused in the photocatalytic process. The DRS and photocurrent analyses indicated that the enhanced Hg^0 removal efficiency over $AgI_{0.3}BiOI/CFO$ could be ascribed to the synergistic effect between AgI, BiOI and $CoFe_2O_4$ under FSL irradiation, which could lead to an efficient e^-–h^+ pairs separation and much more photogenerated reactive species. The trapping experiment result indicated the $^{\bullet}O_2^-$ and h^+ radicals were the primary reactive substances contributing to the oxidation of Hg^0. This work can improve the insight into the wet photocatalytic oxidation process of Hg^0 using magnetic photocatalyst under FSL irradiation and serve as a guide in using magnetic photocatalyst in the field of flue gas treatment.

Acknowledgements

This study was financially supported by the National Natural Science Foundation of China (No. 51676064, 51306046, and 51576086), the Fundamental Research Funds for the Universities of Henan Province (No. NSFRF140204) and the Young Core Instructor Project in the Higher Education Institutions of Henan Province (No. 2016GGJS-038).

References

1 A. P. Dastoor and Y. Larocque, *Atmos. Environ.*, 2004, **38**, 147–161.
2 E. G. Pacyna, J. M. Pacyna, K. Sundseth, J. Munthe, K. Kindbom, S. Wilson, F. Steenhuisen and P. Maxson, *Atmos. Environ.*, 2010, **44**, 2487–2499.
3 X. Zhang, B. X. Shen, S. W. Zhu, H. Xu and L. H. Tian, *J. Hazard. Mater.*, 2016, **320**, 556–563.
4 S. J. Zhao, Z. Qu, N. Q. Yan, Z. Li, W. F. Zhu, J. pan, J. F. Xu and M. D. Li, *RSC Adv.*, 2015, **5**, 30841–30850.

5 State Environmental Protection Administration of China (SEPA), *Emission Standard of Air Pollution for Thermal Power Plants, GB 13223-2011*, Beijing, 2011.
6 C. F. You and X. C. Xu, *Energy*, 2010, **35**, 4467–4472.
7 K. C. Galbreath and C. J. Zygarlicke, *Fuel Process. Technol.*, 2000, **65**, 289–310.
8 R. K. Srivastava, N. Hutson, B. Martin, F. Princiotta and J. Staudt, *Environ. Sci. Technol.*, 2006, **40**, 1385–1393.
9 F. M. Zhan, C. T. Li, G. M. Zeng, S. S. Tao, Y. J. Xiao, X. Zhang, L. K. Zhao, J. Zhang and J. F. Ma, *Chem. Eng. J.*, 2013, **232**, 81–88.
10 Y. X. Liu, J. Zhang and J. F. Pan, *Energy Fuels*, 2014, **28**, 2135–2143.
11 Y. Zhao, R. L. Hao, P. Zhang and S. H. Zhou, *Fuel*, 2014, **136**, 113–121.
12 N. D. Hutson, R. Krzyzynska and R. K. Srivastava, *Ind. Eng. Chem. Res.*, 2008, **47**, 5825–5831.
13 H. Q. Wang, S. Y. Zhou, L. Xiao, Y. J. Wang, Y. Liu and Z. B. Wu, *Catal. Today*, 2011, **175**, 202–208.
14 Y. Li and C.-Y. Wu, *Environ. Sci. Technol.*, 2006, **40**, 6444–6448.
15 J. Wu, C. E. Li, X. Y. Zhao, Q. Wu, X. M. Qi, X. T. Chen, T. Hu and Y. Cao, *Appl. Catal., B*, 2015, **176–177**, 559–569.
16 Y. Yuan, J. Y. Zhang, H. L. Li, Y. Li, Y. C. Zhao and C. G. Zheng, *Chem. Eng. J.*, 2012, **192**, 21–28.
17 X. M. Qi, M. L. Gu, X. Y. Zhu, J. Wu, H. M. Long, K. He and Q. Wu, *Chem. Eng. J.*, 2016, **285**, 11–19.
18 G. P. Dai, J. G. Yu and G. Liu, *J. Phys. Chem. C*, 2012, **116**, 15519–15524.
19 Y. P. Bi, S. X. Ouyang, N. Umezawa, J. Y. Cao and J. H. Ye, *J. Am. Chem. Soc.*, 2011, **133**, 6490–6492.
20 C. Hu, T. W. Peng, X. X. Hu, Y. L. Nie, X. F. Zhou, J. H. Qu and H. He, *J. Am. Chem. Soc.*, 2010, **132**, 857–862.
21 X. Zhang, Z. H. Ai, F. L. Jia and L. Z. Zhang, *J. Phys. Chem. C*, 2008, **112**, 747–753.
22 H. F. Cheng, B. B. Huang, Y. Dai, X. Y. Qin and X. Y. Zhang, *Langmuir*, 2010, **26**, 6618–6624.
23 M. Cui, J. X. Yu, H. J. Lin, Y. Wu, L. H. Zhao and Y. M. He, *Appl. Surf. Sci.*, 2016, **387**, 912–920.
24 A. C. Zhang, L. X. Zhang, X. Z. Chen, Q. F. Zhu, Z. C. Liu and J. Xiang, *Appl. Surf. Sci.*, 2017, **392**, 1107–1116.
25 G. C. Xi, B. Yue, J. Y. Cao and J. H. Ye, *Chem.–Eur. J.*, 2011, **17**, 5145–5154.
26 W. Wu, C. Z. Jiang and V. A. L. Roy, *Nanoscale*, 2015, **7**, 38–58.
27 T. W. Ng, L. S. Zhang, J. S. Liu, G. H. Huang, W. Wang and P. K. Wong, *Water Res.*, 2016, **90**, 111–118.
28 Y. G. Xu, T. Zhou, S. Q. Huang, M. Xie, H. P. Li, H. Xu, J. X. Xia and H. M. Li, *RSC Adv.*, 2015, **5**, 41475–41483.
29 W. Q. Zhang, M. Wang, W. J. Zhao and B. Q. Wang, *Dalton Trans.*, 2013, **42**, 15464–15474.
30 A. Ren, C. B. Liu, Y. Z. Hong, W. D. Shi, S. Lin and P. Li, *Chem. Eng. J.*, 2014, **258**, 301–308.
31 T. P. Xie, L. J. Xu, C. L. Liu, J. Yang and M. Wang, *Dalton Trans.*, 2014, **43**, 2211–2220.
32 Y. S. Fu, H. Q. Chen, X. Q. Sun and X. Wang, *Appl. Catal., B*, 2012, **111–112**, 280–287.
33 R. Jiang, H.-Y. Zhu, J.-B. Li, F.-Q. Fu, J. Yao, S.-T. Jiang and G.-M. Zeng, *Appl. Surf. Sci.*, 2016, **364**, 604–612.
34 S. Duangjam, K. Wetchakun, S. Phanichphant and N. Wetchakun, *Mater. Lett.*, 2016, **181**, 86–91.
35 P. Sathishkumar, N. Pugazhenthiran, R. V. Mangalaraja, A. M. Asiri and S. Anandan, *J. Hazard. Mater.*, 2013, **252–253**, 171–179.
36 S. Singh and N. Khare, *Mater. Lett.*, 2015, **161**, 64–67.
37 L. Q. Jing, Y. G. Xu, S. Q. Huang, M. Xie, M. Q. He, H. Xu, H. M. Li and Q. Zhang, *Appl. Catal., B*, 2016, **199**, 11–22.
38 L. Kong, Z. Jiang, T. C. Xiao, L. F. Lu, M. O. Jones and P. P. Edwards, *Chem. Commun.*, 2011, **47**, 5512–5514.
39 A. R. Upreti, Y. Li, N. Khadgi, S. Naraginti and C. Zhang, *RSC Adv.*, 2016, **6**, 32761–32769.
40 H. G. Kim, P. H. Borse, J. S. Jang, E. D. Jeong, O. S. Jung, Y. J. Suhd and J. S. Lee, *Chem. Commun.*, 2009, **39**, 5889–5891.
41 J. C. Colmenares and R. Luque, *Chem. Soc. Rev.*, 2014, **43**, 765–778.
42 D. H. Xia, L. L. Hu, C. He, W. Q. Pan, T. S. Yang, Y. C. Yang and D. Shu, *Chem. Eng. J.*, 2015, **279**, 929–938.
43 B. Cai, M. G. Zhao, Y. Ma, Z. Z. Ye and J. Y. Huang, *ACS Appl. Mater. Interfaces*, 2015, **7**, 1327–1333.
44 D. A. Reddy, J. Choi, S. Lee, R. Ma and T. K. Kim, *RSC Adv.*, 2015, **5**, 67394–67404.
45 J. L. Liang, C. Shan, X. Zhang and M. P. Tong, *Chem. Eng. J.*, 2015, **279**, 277–285.
46 H. Liu, W. R. Cao, Y. Su, Y. Wang and X. H. Wang, *Appl. Catal., B*, 2012, **111–112**, 271–279.
47 J. Cao, Y. J. Zhao, H. L. Lin, B. Y. Xu and S. F. Chen, *J. Solid State Chem.*, 2013, **206**, 38–44.
48 J.-C. Wang, H.-C. Yao, Z.-Y. Fan, L. Zhang, J.-S. Wang, S.-Q. Zang and Z.-J. Li, *ACS Appl. Mater. Interfaces*, 2016, **8**, 3765–3775.
49 T. Yan, H. Y. Liu, P. C. Gao, M. Sun, Q. Wei, W. G. Xu, X. D. Wang and B. Du, *New J. Chem.*, 2015, **39**, 3964–3972.
50 H. L. Wang, L. S. Zhang, Z. G. Chen, J. Q. Hu, S. J. Li, Z. H. Wang, J. S. Liu and X. C. Wang, *Chem. Soc. Rev.*, 2014, **43**, 5234–5244.
51 A. L. Linsebigler, G. Lu and J. T. Yates, *Chem. Rev.*, 1995, **95**, 735–758.
52 R. F. Dong, B. Z. Tian, C. Y. Zeng, T. Y. Li, T. T. Wang and J. L. Zhang, *J. Phys. Chem. C*, 2013, **117**, 213–220.
53 F. Dong, Y. J. Sun, M. Fu, Z. B. Wu and S. C. Lee, *J. Hazard. Mater.*, 2012, **219–220**, 26–34.
54 Z. H. Ai, W. K. Ho, S. C. Lee and L. Z. Zhang, *Environ. Sci. Technol.*, 2009, **43**, 4143–4150.
55 M. Sun, D. Z. Li, Y. B. Chen, W. Chen, W. J. Li, Y. H. He and X. Z. Fu, *J. Phys. Chem. C*, 2009, **113**, 13825–13831.

